Bull. Mater. Sci., Vol. 36, No. 4, August 2013, pp. 521–533. © Indian Academy of Sciences.

Fast response time alcohol gas sensor using nanocrystalline F-doped SnO_2 films derived via sol–gel method

SARBANI BASU, YEONG-HER WANG†, C GHANSHYAM* and PAWAN KAPUR
CSIR-Central Scientific Instruments Organisation, Sector-30, Chandigarh 160 030, India
†Department of Electrical Engineering, National Cheng Kung University, Tainan 70101, Taiwan

MS received 22 September 2011; revised 25 June 2012

Abstract. **Pure and fluorine-modified tin oxide (SnO_2) thin films (250–300 nm) were uniformly deposited on corning glass substrate using sol–gel technique to fabricate SnO_2-based resistive sensors for ethanol detection. The characteristic properties of the multicoatings have been investigated, including their electrical conductivity and optical transparency in visible IR range. Pure SnO_2 films exhibited a visible transmission of 90% compared with F-doped films (80% for low doping and 60% for high doping). F-doped SnO_2 films exhibited lower resistivity ($0{\cdot}12 \times 10^{-4}$ Ω cm) compared with the pure ($14{\cdot}16 \times 10^{-4}$ Ω cm) one. X-ray diffraction and scanning electron microscopy techniques were used to analyse the structure and surface morphology of the prepared films. Resistance change was studied at different temperatures (523–623 K) with metallic contacts of silver in air and in presence of different ethanol vapour concentrations. Comparative gas-sensing results revealed that the prepared F-doped SnO_2 sensor exhibited the lowest response and recovery times of 10 and 13 s, respectively whereas that of pure SnO_2 gas sensor, 32 and 65 s, respectively. The maximum sensitivities of both gas sensors were obtained at 623 K.**

Keywords. **F-doped SnO_2; sol–gel; gas sensor; sensitivity.**

1. Introduction

Ethanol is the most popular alcohol, best known as the type of alcohol used in alcoholic beverages. Ethanol is produced primarily by fermentation and the vast majority of ethanol produced is used as fuel. The development of a highly sensitive ethanol sensor is desired to control drunken driving and monitor fermentation and other chemical industry processes. The development of ethanol sensors based on thin film technology offers the advantages of exhibiting greater sensitivity (Varghese *et al* 1999). Over the past decades, metal oxide semiconductors have been investigated extensively for sensing various types of vapours and toxic gases (Steffes *et al* 2000; Aukkaravittayapun *et al* 2006; Epifani *et al* 2006; Donato *et al* 2009). Several parameters of materials have been used in gas sensor applications, i.e. adsorption ability, catalytic activity, sensitivity and thermodynamic stability. Among the various metal oxides studied for gas sensor applications, SnO_2 has emerged as one of the potential materials with a wide bandgap (3·6 eV), given its suitable physicochemical properties including high response, stability and reactivity to reducing gases, such as ethanol, as well as a low production cost (Mishra *et al* 2002; Korotcenkov and Cho 2009).

Tin oxide with such unique properties as good transparency and conduction, has found widespread applications. SnO_2 can be engineered into a conductor without affecting its visible transmission. The conductivity arises from oxygen vacancies, the concentrations of which are usually difficult to control. However, the specified addition of group V elements (fluorine or antimony) increases the conductivity of pure SnO_2 film from a normal semiconductor into a degenerate one (Chatterjee *et al* 2003; Han *et al* 2005). Its electrical properties can be explained in two ways: the donor impurity may be connected with oxygen vacancies:

$$SnO_2 \rightleftarrows Sn^{4+} + (2-\varepsilon)\,O^{--} + \varepsilon V^{--} + \varepsilon/2O_2,$$

where V represents vacancies in the anionic lattice or with interstitial tin atoms (Leja *et al* 1979):

$$SnO_2 \rightleftarrows (1-\varepsilon)\,Sn^{4+} + \varepsilon Sn^{o} + (2-2\varepsilon)\,O^{--} + \varepsilon O_2.$$

Tin dioxide becomes a degenerate semiconductor when doped with fluorine (F). The mechanism of the formation of donors is represented as follows (Lampert 1982):

$$xF^{-} + xe^{-} + SnO_2 \rightleftarrows \left(Sn^{4+} + xe^{-}\right) F_xO_{2-x} + xO^{--}.$$

Consequently, an electron is introduce into the conduction band for each F ion. The reduction of the grain size to nanostructure dimensions can largely enhance gas sensor performance (Li *et al* 2004; Chang *et al* 2008). The conductivities of such materials change due to grain coalescence and porosity, as well as grain boundary alteration (Yamazoe 1991;

*Author for correspondence (dcghan@gmail.com)

Xu *et al* 1991). Dopants are used as catalysts in the fabrication of gas sensors to obtain a faster response from the device and to make it more selective towards a given gas (Chaudhary *et al* 1999). The catalyst influences the reaction rate at the sensor–gas interface and modifies the intrinsic physical properties of SnO_2. In particular, the catalyst can modify: (i) the electrical transport properties of the sensor by introducing new states in the band structure of SnO_2, (ii) the surface morphology of the material, a very important property influencing the number of surface sites available for chemical reactions to take place between sensor and gas and (iii) the size of SnO_2 crystalline grains, which are closely connected to electrical properties of the material, because it helps to determine the electrical resistance of the material. With respect to other techniques, the dopant is typically already introduced in the starting solution during the sol–gel process, thus, it is distributed throughout the final material. Higher ratios of dopants may result in a modification of the electrical conductivity of the sensor, which decreases sensor sensitivity (Han *et al* 2005). SnO_2-based gas sensors are fabricated in various forms as a thin (Park and Mackenzie 1996) or thick film (Vlachos *et al* 1995). Each process has its advantages and drawbacks in terms of implementation complexity and film quality. Various methods, such as sputtering, chemical vapour deposition and sol–gel derivation have been developed to fabricate such films. The properties of the films strongly depend on the preparation method. The sol–gel technique has several advantages, including simple and low-cost processing, precise control of doping level, capability to coat large and complex shapes and a porous structure desirable for gas sensor applications. To the best of our knowledge, few reports describing the synthesis of nanocrystalline F-doped SnO_2 and its application to micro-gas sensors are available (Han *et al* 2005, 2006). SnO_2 films are sometimes doped with palladium and platinum to improve the selectivity and sensitivity of gas sensors (Esfandyarpour *et al* 2004; Chen *et al* 2010). F-doped tin oxide thin films have been successfully demonstrated as transparent conductors, optical windows for solar spectrum, light emitting diodes and many more. The conductivity of SnO_2 films can be enhanced by appropriate doping. In addition, F-doped SnO_2 films have higher conductivity than undoped SnO_2 films. Han *et al* (2005, 2006) previously reported a gas sensor system using micro-electro mechanical system (MEMS) technology for coating the nanocrystalline F-doped SnO_2 based on Si substrate with platinum electrode (Han *et al* 2005). However, the sensitivity to 100 ppm hydrogen gas at a heater voltage of 0·7 V was as low as 2·8. The low sensitivity was due to the low resistivity of F-doped SnO_2 ($\sim$1·8 Ω cm). Thus, various techniques have been applied to modify the sensing properties of gas sensors. One significant approach was modifying the metal oxide surface using a catalyst layer or gas filter layer. Shukla *et al* (2005a, b) have recently investigated the effect of air pressure, ultraviolet radiation exposure, as well as the inverse catalytic effect at lower operating temperatures, on the sensing characteristics of the sensors. Wada and Egashira (2000) have reported that electrical resistance of SnO_2 sensors in air increased slightly with the amount of SiO_2 on SnO_2 surface.

This study sought to explore the synthesis of nanocrystalline F-doped SnO_2 and its application as an ethanol gas sensor. In addition, this study aims to evaluate the sensitivity of F-doped SnO_2 gas sensor prepared via low cost sol–gel technique compared with conventional SnO_2 sensor for ethanol gas detection. The most important feature of the present investigations includes fast response and quick recovery time. A comparative study of various structural, optical and electrical properties of F-doped SnO_2 and pure SnO_2 films were studied. Furthermore, these films were tested for their sensitivity, response time and recovery time in the presence of ethanol gas at a temperature range of 523–623 K. The sensitivity of F-doped SnO_2 sensor did not show much improvement compared with pure SnO_2 sensor. This gas sensor may show higher sensitivity and better selectivity for hydrogen gas compared with commercially available SnO_2 gas sensors similar to a previous research (Han *et al* 2005).

2. Experimental

The following procedures were used to prepare pure and modified SnO_2 thin films using sol–gel and spin-coating techniques. Sol preparation and its stability are essential to obtain a reproducible final product. Corning glass (7059) slides were used as substrates. The substrates were cleaned thoroughly in liquid detergents and distilled water followed by boiling in distilled water. The substrates were then subjected to ultrasonic treatment in 2-propanol for 15 min and degreased with 2-propanol vapour before drying. Analytical reagent grade $SnCl_2{\cdot}2H_2O$ was used as starting material. Sol–gel SnO_2 was prepared using the procedure described by a previous study (Elangovan *et al* 2004). $SnCl_2{\cdot}2H_2O$ (11 g) was dissolved in concentrated HCl by heating at 363 K for 10 min and subsequently diluted with ethanol to form the starting solution. Stirring was continued until the cooling process was completed and $SnCl_2$ solution was then aged for 48 h at room temperature. Different dopant concentrations of NH_4F in $SnCl_2{\cdot}2H_2O$ at F/Sn ratios of 1·5, 1 and 0·5 M were used for F-doping. NH_4F dissolved in double-distilled water was added to the starting solution. Different amounts of NH_4F were mixed with a constant amount of water (water/Sn molar ratio of 10). The prepared sol (NH_4F and $SnCl_2$) was then spin-coated over the glass substrate to obtain F-doped SnO_2 multilayer samples. The film was immediately annealed at 373 K for 10 min in air and then allowed to cool at room temperature to produce a transparent and adherent films. Multilayered films (starting from 1 layer to 5 layers) were prepared using the above procedure. Every layer was deposited, repeating the same procedure and conditions as previously described. The films were deposited onto corning glass (7059) substrates and were finally annealed at a temperature range of 723–873 K. Spin-coating speed, annealing temperature and time are important parameters in

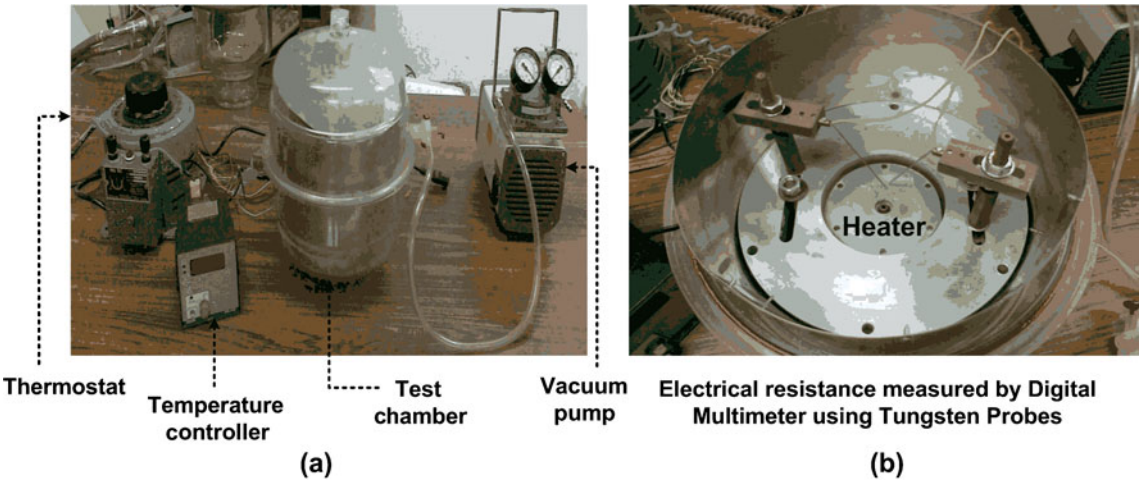

Figure 1. (**a**) Entire gas sensor testing chamber set up consisting of thermostat, heater, temperature controller, vacuum pump, two tungsten electrode probes and digital multimeter and (**b**) internal parts of testing chamber showing two electrodes used for film resistance measurement. Output of two electrodes were connected to multimeter.

controlling film thickness. SnO_2 film thickness in all our measurements was maintained between 250 and 300 nm.

The characteristic properties of multi-coatings were investigated with respect to their electrical conductivity and optical transparency in visible IR range. Electrical resistivity and Hall effect measurements were carried out on the samples using van der Pauw configuration. Surface morphology was investigated by field emission scanning electron microscopy (FESEM JEOL JSM 6700 with a beam voltage of 15 kV). Crystal phases in the annealed thin films were studied using X-ray diffractometer (X'Pert Panalytical) operated at 40 kV, 30 mA over 20–70° with a scan rate of 0·002°/s. X-ray diffraction (XRD) using CuKα line was used to analyse the structure of the prepared films. The crystallinity of each film was calculated from XRD spectra using Scherrer formula:

$$D_m = 0{\cdot}9\lambda/(\beta \cos\theta),$$

where D_m is the crystallite size, β the full width at half maximum of a distinctive peak (rad), θ the Bragg angle and $\lambda = 0{\cdot}154$ nm (CuKα). Optical studies were performed by measuring transmittance and absorbance in the wavelength region, λ = 200–3500 nm at room temperature using a spectrophotometer (Hitachi-U3410).

Sensitivity tests were carried out in a homemade testing chamber that measures the surface resistance of the samples (figure 1). The testing chamber consisted of a stainless steel base with multiple holes at the side for the insertion of more than one gas at a time. Heater temperature was increased by regulating the thermostat voltage and sensor temperature was monitored by the thermocouple. The output of the thermocouple was connected to the digital temperature indicator. The sample was pre-heated and cooled 3–4 times before the measurement to remove water vapour from SnO_2 film. Ethanol was injected into the test chamber using a microsyringe. N_2 air was allowed to pass into the glass chamber before the start of a new gas exposure cycle. The required gas concentration was calculated from the known chamber volume. One part per million (by volume) is equal to a volume of a given gas mixed in million volumes of air. The glass substrate with SnO_2 film placed above the heater was connected by two probes, which were further connected in a series with a digital multimeter. It can measure the electrical resistance change of the film after gas exposure. Resistance values were determined to obtain the gas response. Sensitivity, S, was expressed in terms of sensor resistance in air (R_a) and in test gas (R_g) as follows: $S = R_a/R_g$. The whole system was covered by a glass chamber fitted with a rubber tube at the base to ensure a complete vacuum inside the chamber through suction using a vacuum pump. Response time is defined as the time to reach 90% saturation response. Recovery time is the time taken by the sensor to recover 90% of the maximum resistance when the gas flow is switched off.

3. Material characterization

Surface morphologies of pure and F-doped SnO_2 films obtained through scanning electron microscopy (SEM) are shown in figure 2. Figures 2(a) and (b) show pure SnO_2 film at annealing temperatures of 773 and 823 K, respectively. These films were compact. Figures 2(c)–(e) show typical scanning electron micrographs of three representatives of SnO_2 films with increasing amounts of F. These films were annealed at 773 K. The doped films exhibited a fine-grained surface. Grain growth increased with increasing F content. No measurable change was observed in average grain size neither by changing the film thickness (100–300 nm) nor by annealing pure SnO_2 films for various durations. However, the surface became rougher with increasing precursor content. Based on SEM study, the average grain size for high-doped film was measured between 200 and 250 nm. Moreover, pure SnO_2 coatings did not show any detectable cracks, holes or grains.

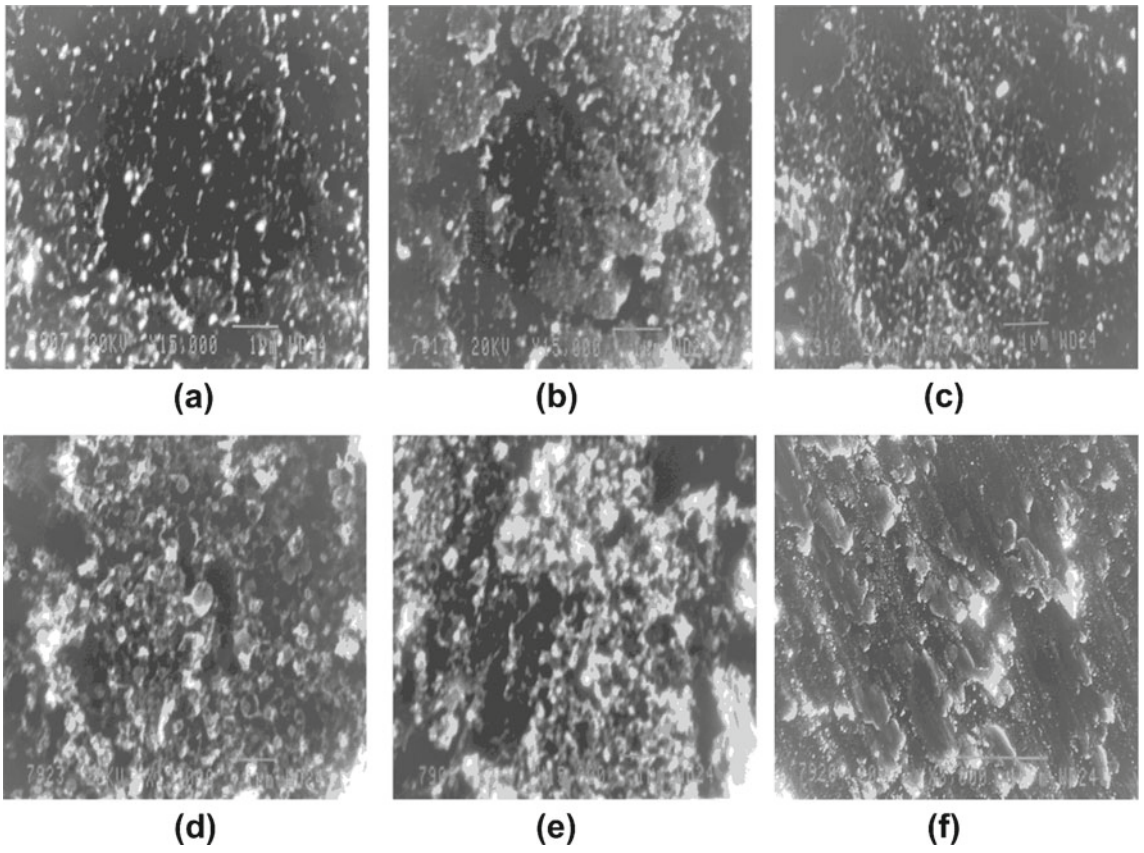

Figure 2. SEM images for pure SnO_2 films annealed at (**a**) 773 K and (**b**) 823 K prepared sol–gel process. (**c**)–(**f**) Typical surface morphologies of F-doped SnO_2 films with an increasing amount of F. These films were annealed at 773 K for 30 min in ambient temperature at different F/Sn molar ratios in SnO_2 lattice; (**c**) 0·5 (low-doped), (**d**) 1·0 (medium-doped), (**e**) 1·5 (high-doped) and (**f**) only one upper layer doped with F (F/Sn ~1·5) were spin-coated on SnO_2 surface.

Figures 3(a)–(c) show surface morphology of low-, medium- and high-doped SnO_2 films, respectively. However, these F-doped SnO_2 films annealed at 873 K showed grain or nanoparticle growth throughout the film surface. Figure 3(d) demonstrates the film with cracks, which may be attributed to higher film thickness. These superficial cracks appear as the films shrink because of grain growth during the calcination process. Presumably, such cracks remain superficial and do not penetrate through the film as suggested in Sakai *et al* (2001).

X-ray diffraction studies were carried out using an X'Pert Pro instrument. A full range of scanning was performed for the scanning angle (2θ). X-ray diffraction patterns of the five-layered SnO_2 thin films for sols were obtained. Figure 4 shows X-ray diffraction pattern of SnO_2 film deposited using the sol–gel method. The different structures of the film were analysed by preparing four samples (a–d) and applying four different conditions on these samples. Sample (b) was annealed at 723 K for 30 min in air, whereas sample (c) was annealed at a higher temperature of 773 K for 30 min in air. The crystallite size of the samples annealed at temperatures 723 and 773 K were calculated using Scherrer formula and were found as 8·9 and 13·86 nm, respectively indicating their nanocrystalline nature. XRD of high-temperature annealed film revealed sharper peaks compared with lower-temperature annealed samples. Thus, grain and crystalline sizes were improved at high temperature annealing. XRD spectra of the deposited SnO_2 films show reflection from (110), (101), (200) and (211) planes of SnO_2 for 2θ values of 26·52, 33·72, 37·81 and 51·87°. Sample (a) was prepared after ethanol gas exposure as pure sample and annealed at 723 K; whereas sample (d) was doped with F and annealed at 773 K. Reflections from the tetragonal crystallographic phase (cassiterite structure, JCPDS 41-1445) without any impurity of SnO_2 were more defined, progressively sharper and more intense for F-doped SnO_2 film. The crystallite size of F-doped film increased to 23·80 nm, which may be attributed to the improved crystallinity and increased small crystallite agglomeration. These agglomerated crystallites coalesce together, resulting in the formation of larger grains with better crystallinity. The presence of other orientations such as (310), (301) and (321) were also detected with considerable intensities for pure and doped films (Han *et al* 2005). However, diffraction patterns of F-doped films did not show any appreciable changes from those of pure films, which may be a result of low F concentration in the film.

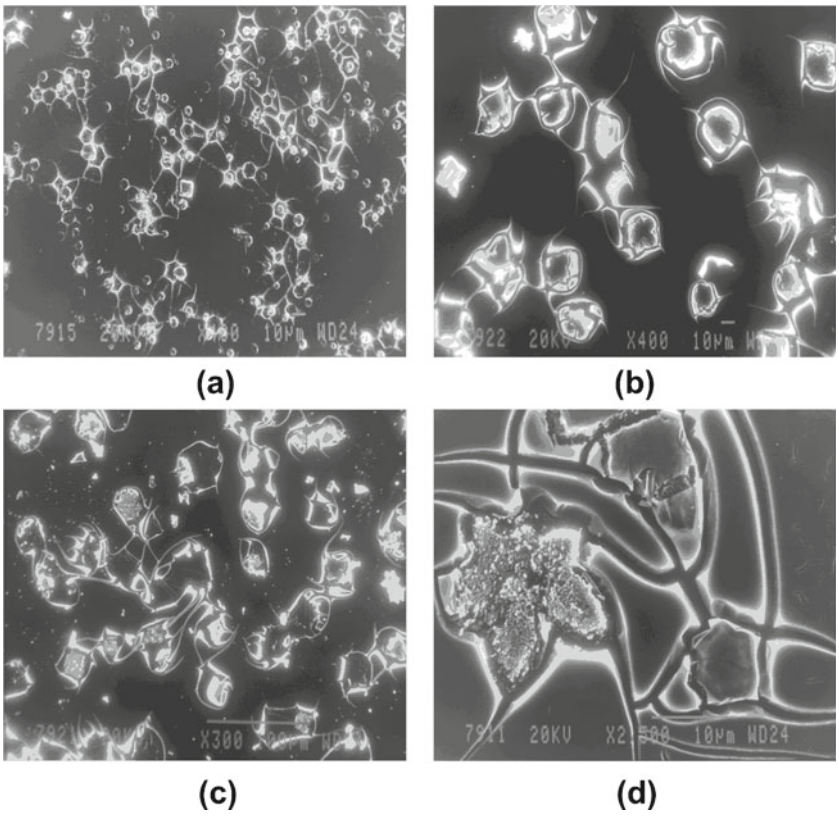

Figure 3. SEM images for different F/Sn molar ratios annealed at 873 K for 30 min. (**a**) F/Sn ∼ 0·5, (**b**) 1·0, (**c**) 1·5 and (**d**) thick F-doped SnO_2 film with a thickness of ∼1 μm.

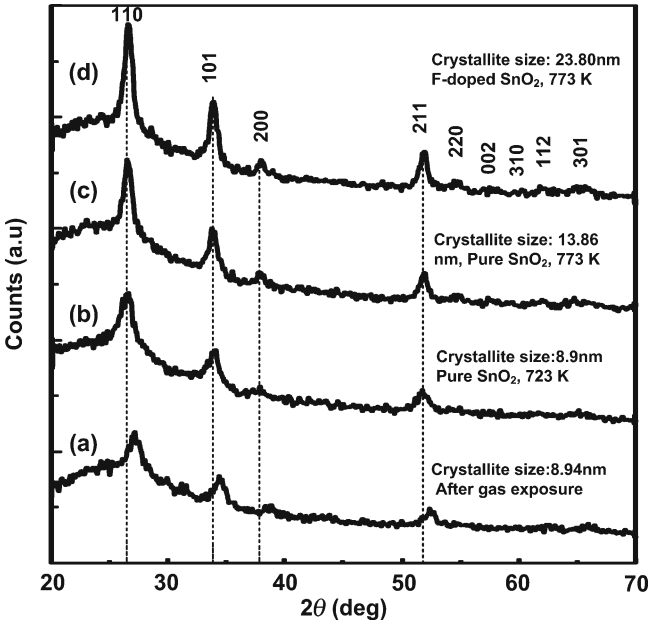

Figure 4. XRD results of pure SnO_2 films (samples **a**, **b** and **c**) and F-doped SnO_2 films (sample **d**) deposited sol–gel process on corning glass substrate at varying annealing temperatures. Samples (**a**) after ethanol gas exposure, (**b**) annealed at 723 K, (**c**) annealed at 773 K and (**d**) F-doped SnO_2 thin films annealed at 773 K.

The crystallite size of ethanol-exposed sample was 8·94 nm. No change was observed in the nanocrystallite size after gas exposure indicating that point defect distribution within the nanocrystals remained constant.

4. Electrical data of pure and F-doped SnO_2 films

Table 1 shows comparison of electrical data obtained from Hall measurements for the four-point probe method (van der Pauw) for pure and F-doped SnO_2 films with those obtained in previous studies (Gordillo *et al* 1994; Acosta *et al* 1996; Thangaraju 2002; Elangovan and Ramamurthi 2003; Elangovan *et al* 2004). Carrier concentration, carrier mobility and sheet resistance were measured using resistivity measurements at room temperature. The *n*-type electrical conductivity of the films was confirmed by Hall measurement. The resistance of pure SnO_2 sensor was 0·3 MΩ in air at 295 K, which drastically dropped to 50 KΩ under the same conditions, when measured with F-doped SnO_2 sensor. The former sensor exhibited a resistance of 4·5 KΩ upon the introduction of 1000 ppm ethanol at 623 K, whereas F-doped sensor resistance decreased to 0·25 KΩ. The resistivity of F-doped sensor was 118 times lower when compared to pure SnO_2 sensor. The sheet resistance of ∼10–100 Ω/M and high transmittance in the visible region, >80% were

Table 1. Comparison table of electrical data for pure SnO_2 and F-doped SnO_2 films.

Material	Resistivity (Ω-cm) $\times 10^{-4}$	Hall mobility ($cm^2\ V^{-1}S^{-1}$)	Carrier concentration (cm^{-3})	Sheet resistance ($\Omega/\square$)
SnO_2	14·16	46	$5{\cdot}06 \times 10^{15}$	35·4
SnO_2:F	0·12	2·31	$5{\cdot}84 \times 10^{19}$	0·3
This work				
SnO_2	46·3	109·5	$0{\cdot}12 \times 10^{20}$	38·2
SnO_2:F (15 wt%)	2·1	22·1	$13{\cdot}3 \times 10^{20}$	1·8
SnO_2:Sb (2 wt%)	2·9	12·0	$16{\cdot}8 \times 10^{20}$	2·2
Elangovan *et al* (2004)				
SnO_2:F				
(15 wt%)	1·4			1·75
(20 wt%)	2·54	–	–	3·18
(5 wt%)	3·68			4·61
Elangovan and Ramamurthi (2003)				
SnO_2:F (10 wt%)	1	9·6	$5{\cdot}7 \times 10^{20}$	5·65
Thangaraju (2002)				
SnO_2:F				
(4·5 wt%)	6	–	$1{\cdot}1 \times 10^{21}$	16·40
(>15 wt%)	19		$2{\cdot}7 \times 10^{21}$	97·43
(30 wt%)	46		$3{\cdot}3 \times 10^{21}$	127·77
Acosta *et al* (1996)				
SnO_2:F				
(0·7 mole%, $SnCl_4$)	4	–	–	5·33
(1·1 mole%, $SnCl_2$)	2·5			3·33
Gordillo *et al* (1994)				

useful for transparent electrodes in liquid crystal and photovoltaic devices, whereas high sheet resistance of $\sim 10^4$–10^8 of SnO_2 films did not allow for transparent electrodes. A carrier concentration of $5{\cdot}06 \times 10^{15}$ cm^{-3} was associated with a mobility of 46 $cm^2\ V^{-1}\ S^{-1}$ for pure SnO_2 film. The corresponding values of F-doped films were $5{\cdot}84 \times 10^{19}$ cm^{-3} and 2·31 $cm^2\ V^{-1}\ S^{-1}$, respectively. These results are close and comparable to those obtained with sprayed FTO film (Elangovan *et al* 2004). The heavily doped films are degenerated and exhibited *n*-type electrical conductivity. Film degeneracy was established by evaluating Fermi energy by the expression:

$$E_F = \left(h^2/8m^*\right)\left(3n/\Pi\right)^{2/3},$$

where h is the Planck's constant, n the concentration of free carrier and m^* the reduced effective mass.

The undoped SnO_2 films contained oxygen vacancies. It is common that some of the oxygen vacancies have been filled by the precursor solution containing $SnCl_4{\cdot}2H_2O$. When the dopant was incorporated at oxygen vacancies, the drop in carrier concentration takes place, however, if it replaced oxygen, an increase in carrier concentration will be observed. In case of fluorine-doped SnO_2 films, the value of sheet resistance were decreased due to each F^- anion substituted an O^{2-} anion and created more free electrons. Once the equivalent number of oxygen vacancies were filled, the dopant will enter SnO_2 lattice substitutionally. This substitution depended upon the ionic size and charge of the particular dopant. The ionic size of fluorine ($F^- \sim 0{\cdot}133$ nm) was very close to the value of oxygen ($O^{2-} \sim 0{\cdot}132$ nm). The energy of Sn–F bond ($\sim 26{\cdot}75°$ D/kJmol^{-1}) was comparable to that of Sn–O bond ($\sim 31{\cdot}05°$ D/kJmol^{-1}). As the charge on fluorine ion was only half of the charge on the oxygen ion, Coulomb forces which bind the lattice together were reduced. It is clear from table 1 that beyond a certain doping level (<15 wt%) of fluorine, the value of sheet resistance was decreased, however, at higher doping level the sheet resistance was increased because of excess fluorine anions. These excess F atoms did not occupy the exact lattice positions and enhanced the disorder of lattice structure. When doping level was going to be higher, the precursor solution (SnO_2:F) turned milky to turbid, which indicated less solubility of F anions. The grain size dependence on dopant concentration was not so effective. According to the charge trapping model (Kamins 1971; Seto 1975), the grain boundary scattering was not the dominant factor for deciding mobility. In this model, the conduction mechanism is based on the thermionic emission over the potential barrier. However, for heavily doped films, the activation energy (barrier energy) was smaller than kT ($\sim 0{\cdot}03$ eV at room temperature), since the resistivity remained nearly constant throughout the temperature range of 300–473 K (Thangaraju 2002). The conductivity of the film was determined by the carrier concentration. Ionized impurity scattering was the dominant

factor limiting mobility of the films since free carriers may interact with a variety of scattering centres (impurity atoms, thermal vibrations of the lattice atoms and structural defects). The presence of ionized impurity scattering was confirmed by Lark–Horovitz relation (Johnson and Horovitz 1947). The mobility due to ionized impurities was estimated by the following expression (Thangaraju 2002).

$$\mu_i = (2/m^*)^{1/2}\left\{\varepsilon E_F^{3/2}\right\}\Big/\{\Pi e^3 f(x) N_i\},$$

where ε is the absolute dielectric permittivity and m^* the effective mass of the carriers, N_i the carrier concentration of ionized impurities.

5. Optical properties

An ultraviolet-visible-near infrared Hitachi 3400 spectrometer was used to measure the reflection spectrum of coated glass for comparison with that of bare glass. Figures 5(a) and (b) present transmittance curves and corresponding reflection curves of pure and F-doped SnO_2 films deposited on corning glass substrates, respectively. The transmittance curves were plotted in the wavelength range of 200–3300 nm. Figure 5(a) shows that the transmittance dropped with higher doping when compared with pure SnO_2 film. Pure SnO_2 film showed a maximum transmittance of more than 85% throughout the wavelength range of 200–3300 nm, whereas transmittance was reduced to 45% from 70% in the same region for high-doped film, because of the increasing thickness of doped film which is suitable for absorbing light. Although the transmittance of high-doped films was lesser, conductivity was considerably better than pure SnO_2 and low-doped films. The films show increased reflectance with increased F-doping at higher wavelengths (>2700 nm) as shown in figure 5(b). The high-doped SnO_2 (F/Sn ~ 1·5 M) film showed a maximum reflectance of 20% at 2700 nm wavelength. However, the reflectance increased slightly when compared with low-doped and pure SnO_2 film. The reflectivity obtained at a wavelength in the visible range was relatively lower at below 10% and the reflection was still low compared with that obtained by Eun and Ko (2003), which reported that the reflection in the infrared region for F-doped SnO_2 glass was better (~70%) and even better for a thicker film (720 nm). Meanwhile, SnO_2:F (15 wt%) thick film of 1·2 μm showed a reflectance value of ~10% at lower wavelength, and a maximum of ~50% at 2500 nm, as described by Elangovan *et al* (2004). High IR reflectivity for a material is desirable, i.e. to be useful for solar energy conversion because the escape of thermal energy in the form of IR radiation considerably reduces the conversion efficiency in flat plate collectors (Mohammed and Abdul Ghafor 1989).

The optical absorption spectra of pure SnO_2 film and the nanostructure of F-doped SnO_2 thin films are shown in figure 6. Absorption increases with increased doping level. Pure SnO_2 film appeared transparent, whereas F-doped SnO_2 films showed poor transparency in the visible range even though they are transparent to the naked eye. NH_4F was dissolved in distilled water and added to pure SnO_2 solution for F doping. Afterwards, the film colour turned from transparent to slightly milky white. The heavy F doping may lead to increased degeneration (metallic) of the films which results in higher light absorption. The optical bandgap energy (E_g) was determined by extrapolating the linear portion of $(\alpha hv)^{1/2}$ vs hv plot. The plot is shown in figure 6(b). The bandgap energies observed for high-doped, medium-doped, low-doped, pure SnO_2 and ethanol-exposed films were calculated from the spectra as 3·1, 3·6, 3·55, 3·45 and 3·35 eV, respectively. Figure 6(b) shows that bandgap energy decreases with increased film doping. This effect may be attributed to the dispersion of F ions in SnO_2 matrix. Increased crystallite size for high doping may be attributed to the improved crystallinity and the agglomeration of small grains or crystallites. The agglomerated grains coalesced to

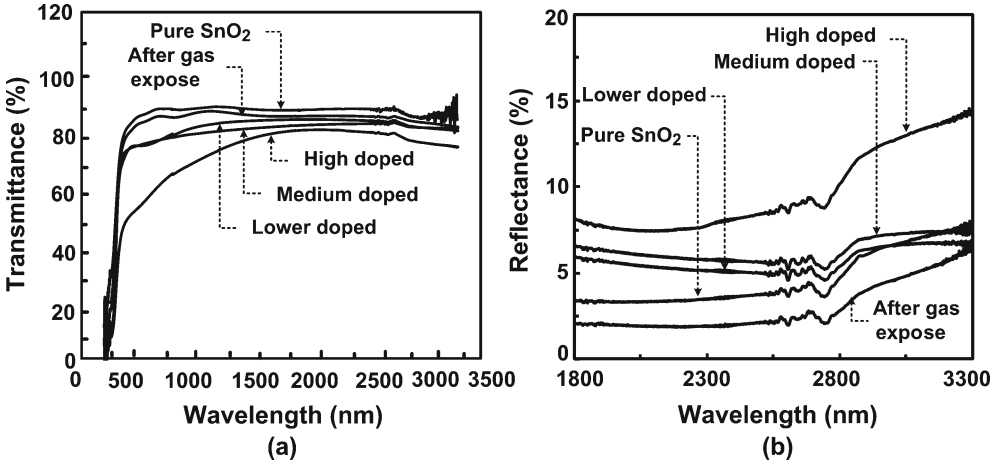

Figure 5. (**a**) Transmittance spectra and (**b**) reflectance spectra of pure, ethanol gas-exposed SnO_2 film, low F-doped (F/Sn = 0·5), medium F-doped (F/Sn = 1·0) and high F-doped (F/Sn = 1·5) SnO_2 thin film deposited on corning glass via sol–gel process. Transmission value decreased with increased F doping.

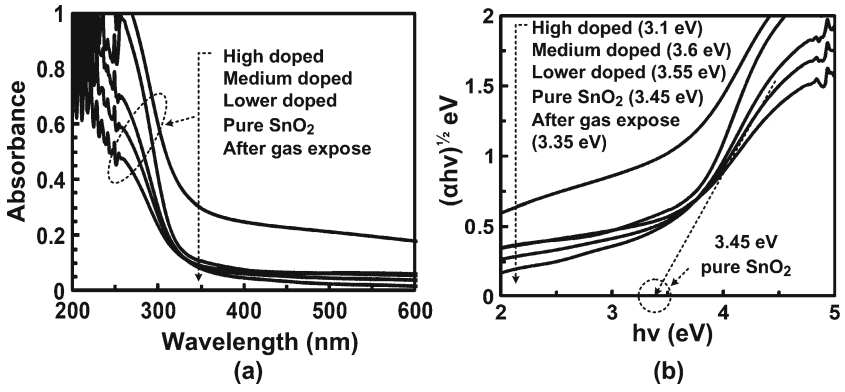

Figure 6. (**a**) Optical absorption spectra of pure and nanostructured F-doped SnO_2 thin films; (**b**) square root of product of absorption coefficient and photon energy vs photon energy for SnO_2 films with different molar preparation of films, such as pure, ethanol gas-exposed, low F-doped (F/Sn = 0·5), medium F-doped (F/Sn = 1·0) and high F-doped (F/Sn = 1·5).

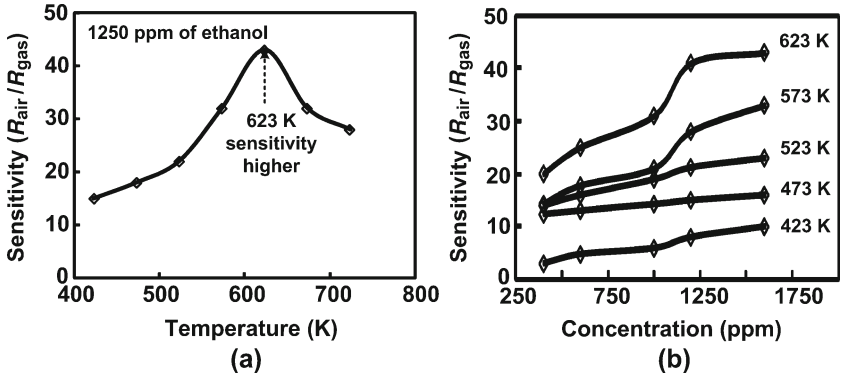

Figure 7. (**a**) Variation in sensitivity of pure SnO_2 thin films with temperature at 1250 ppm ethanol concentration and (**b**) variations in sensitivity with ethanol concentrations at various temperatures.

form a larger grain, which resulted in enhanced crystallinity. This decrease in bandgap may be due to the nanocrystalline nature of the films. The bandgap decreased to 3·45 eV for pure SnO_2 film and to 3·35 eV for ethanol exposed film because of the physisorption of ethanol onto SnO_2 surface and annealing at ∼573 K for a long time while sensitivity tests led to surface-facilitated grain growth. However, the nanostructure size did not change after ethanol gas exposure (shown in XRD study) for pure film. The pure SnO_2 films showed a bandgap energy of 3·45 eV, which was closer to the reported bandgap of SnO_2 (3·6 eV) (Gu *et al* 2000). The bandgap decreased considerably for films with varied thickness.

6. Gas sensor measurements, results and discussion

Systematic gas sensing studies on SnO_2 thin films were made using silver (Ag) contacts. The sensitivity of operating temperature as a function to 1250 ppm ethanol vapour is shown in figure 7(a). Ethanol gas acts as a reducing gas, decreasing the resistance of *n*-type semiconductor metal oxides at elevated temperatures by consuming oxygen adsorbents on the oxide surfaces. The sensitivity evidently increased with operating temperature, reaching a maximum ($S = 45$) at 623 K. Therefore, highest sensitivity was obtained at 623 K. The sensitivity decreased with an increase in temperature above 623 K. This behaviour may be explained based on the kinetics and mechanism of gas adsorption and desorption on SnO_2 or other similar semiconducting metal oxide surfaces. The sensitivity of the sensor depends on two factors. First is the speed of chemical reaction on the grain surface. Second is the speed of gas molecule diffusion to the surface. Sensor response was restricted by the chemical reaction speed at low temperatures. Thus, the adsorption and/or reaction of the gases were reduced, thereby, reducing the removal efficiency of adsorbed oxygen. Meanwhile, adsorption and reaction occurred immediately at higher temperatures.

Thus, complete oxidation of ethanol by chemisorbed oxygen to H_2O was accelerated in air. However, the oxygen re-adsorption was also accelerated at higher temperatures, leading to a smaller change in the surface coverage of oxygen adsorbents. Hence, sensor response was restricted by the diffusion speed of gas molecules to that of surface at higher temperatures. Furthermore, the speed values of the two processes became equal at an intermediate temperature and that particular temperature sensitivity reaches its maximum value. The sensor material surface was covered with chemisorbed oxygen ions, which may be O_2^-, O^- or O^{2-}, depending on the sample temperature. O^{2-} species are highly unstable and do not function significantly in determining sensitivity. Yamazoe *et al* (1979) reported that the highly active O^- was the dominant factor for SnO_2 for temperatures between 473 and 723 K. The major species adsorbed in our film was thus likely to be O^-. Therefore, most of the oxygen species would react with OH group of ethanol vapour at 623 K. According to this mechanism, every gas corresponds to a specific temperature at which the sensitivity attains its peak value. Figure 7(b) shows variation in sensitivity with ethanol concentration at different temperatures ranging from 523 to 623 K. The sensitivity was linear at a concentration range of 375–1000 ppm of ethanol. Sensitivity level reaches its maximum value at 1250 ppm and saturates thereafter. The saturation is due to a deficiency in ionosorbed oxygen species, which can support kinetic mechanisms. An increase in ethanol concentration provides more ethanol molecules to be absorbed on the oxide surface per unit time, thereby favouring fast electron transport kinetics, thereby increasing sensitivity. In addition, further experiments showed that response time decreases at higher concentrations, whereas recovery time is longer due to the slow desorption kinetics of ethanol gas from the interface at higher concentrations.

Figure 8(a) shows time vs sensitivity behaviour of pure SnO_2 sensor at different temperatures. Ethanol gas (1250 ppm) was injected at 523, 573 and 623 K and then flushed out. Sensor sensitivity was higher at higher temperature (623 K) than at lower temperature (523 K) for both sensors. The response and recovery times were also minimum at 623 K. The response times of the pure sensor were 30, 35 and 42 s at 523, 573 and 623 K, respectively whereas its corresponding recovery times were 65, 72 and 88 s at 523, 573 and 623 K, respectively. Figure 8(b) shows that samples collected for sensitivity measurements were considered as higher F-doped. Figure 8(b) also shows that F-doped SnO_2 sensor did not show much higher sensitivity to ethanol gas compared with commercially available SnO_2 sensors. However, some improvements were observed, which may be due to the greater adsorption of ethanol molecules at favourable sites on F atoms of SnO_2 materials or the increased *n*-type property of SnO_2 by F-doping. Although the doping level was high enough, a lower sensitivity for F-modified SnO_2 gas sensors is possible (Han *et al* 2005). A well known critical approach has been done to enhance the sensing properties of the gas sensor, such as modifying the metal oxide surface using a catalyst layer or gas filter layer. The addition of lead or platinum also enhances catalytic activity of the sensor materials.

Sensitivity also increased because of a higher surface-area-to-volume ratio. Thus, surface area was enhanced for F-doped sensors. Recently, Han *et al* (2006) reported that H_2 sensitivity of surface-modified (SiO_2) F-doped SnO_2 microsensor increased and reached $S = 175$, which was found to be about 40 times greater than that of unmodified F-doped SnO_2 sensor. Obviously, the incorporation of SiO_2 is effective for the enhancement of sensor sensitivity to hydrogen due to low conductivity after SiO_2 addition to SnO_2 film. Furthermore, the sensitivities of F-doped SnO_2 sensor for other gases (C_3H_8, CO and CH_4) were relatively low (Han *et al* 2006). This study expects that F-doped sensor shows better selectivity and sensitivity for H_2 gas sensing in the near future. The low sensitivity to ethanol vapour compared with that to H_2 may be due to the smaller molecular size of H_2 molecules.

Figures 9(a) and (b) indicate resistance change at 1250 ppm of ethanol gas for pure and F-doped sensors. Both sensor resistances come to saturation within 75 and 50 s for pure and doped SnO_2 sensors, respectively. Afterwards, no more O^- species would be left to react with ethanol vapour.

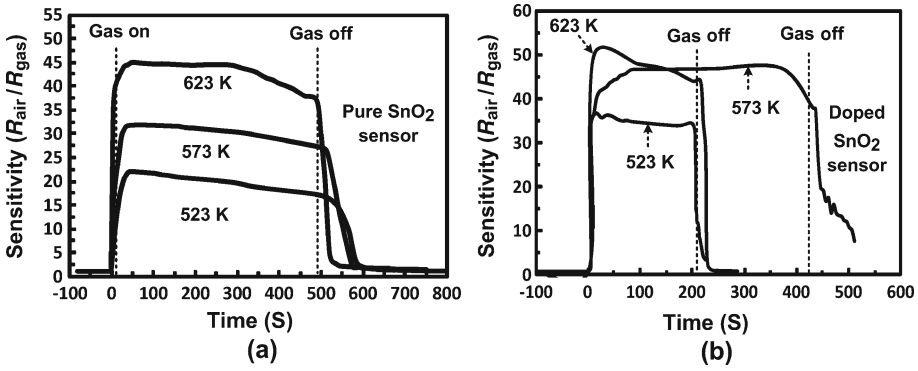

Figure 8. Transient response curves of (**a**) pure SnO_2 sensor and (**b**) F-doped SnO_2 sensor at temperatures 523, 573 and 623 K.

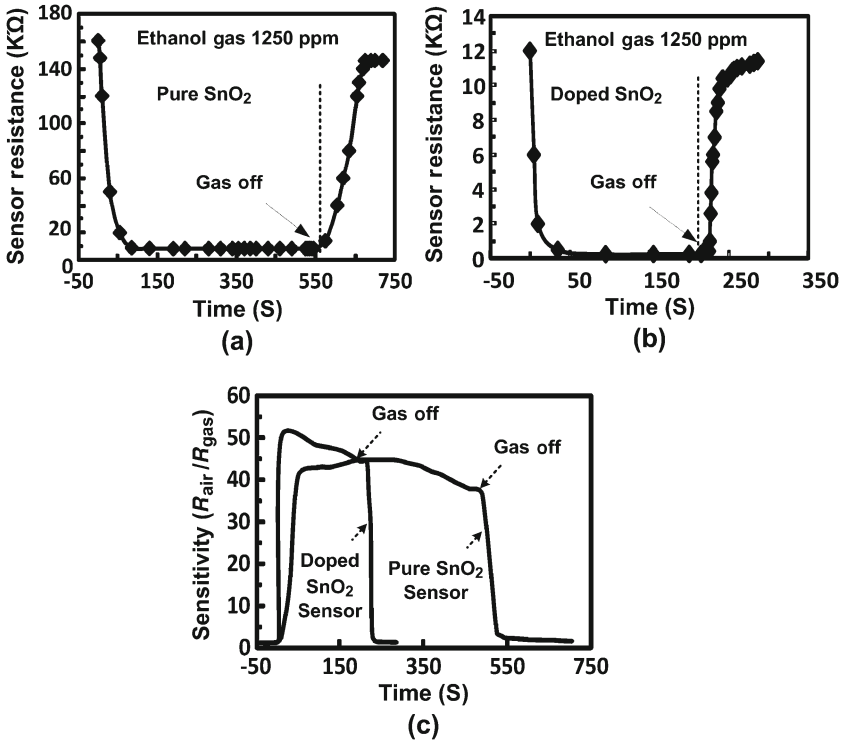

Figure 9. Transient response curves plotting change of resistance values with time. 1250 ppm ethanol gas vapour was injected at 623 K and then flushed out immediately. (**a**) Pure SnO_2, (**b**) F-doped SnO_2 and (**c**) comparison of sensitivity between pure and F-doped SnO_2 gas sensors.

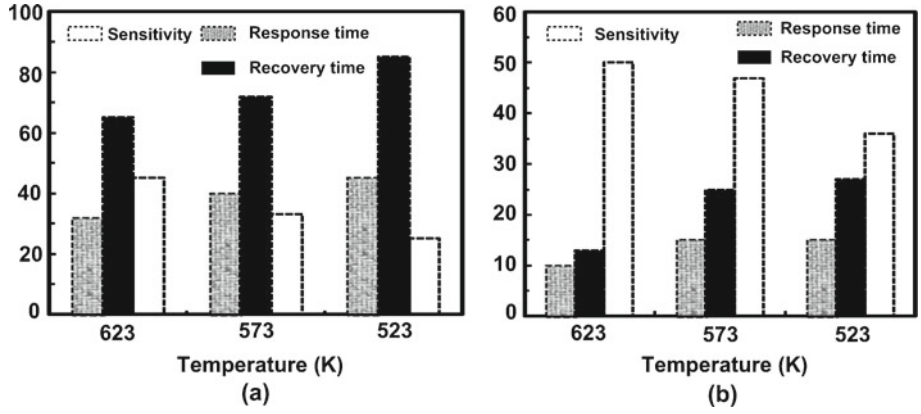

Figure 10. Sensitivity, response time and recovery time as a function of temperature for (**a**) pure and (**b**) F-doped SnO_2 sensors.

The resistance of the sensor initially decreased after exposure to ethanol gas because of the release of free electrons and subsequent saturation; whereas the resistance increased and returned to its baseline value after cutting off the ethanol gas supply. The chamber was refreshed with N_2 air after every new cycle. In particular, electric resistance decreased by about 15 times in magnitude within a minute with F-doped sensors compared with pure sensors at 623 K as indicated in figures 9(a) and (b). The comparative transient response behaviour of both sensor structures is shown in figure 9(c). 1250 ppm ethanol gas was injected at 623 K and then flushed out.

The response time, recovery time and sensitivity of pure and F-doped sensors are shown in figure 10. Figure 10(a) shows that response time of pure SnO_2 sensor is 32 s and recovery time is 65 s. However, F-doped sensor responded

quickly within 10 s and recovered quickly at ∼13 s, as shown in figure 10(b). The response and recovery times were improved in F-doped sensor compared with pure SnO_2 sensor. The negligible quantity of the surface reaction products and high volatility explain the quick response to ethanol vapour and the fast recovery to the baseline value. The response and recovery times decreased with increasing ethanol concentration at a lower working temperature, but do not depend upon ethanol concentration at higher working temperatures. All sensors exhibited relatively quick response to ethanol gas. Reaction rate decreased as temperature decreased, thus, response and recovery times also increased. In summary, the recovery time of F-doped SnO_2 sensors was relatively short, whereas that of pure SnO_2 sensors was long. Doped sensors exhibit similar sensitivity but with faster response and recovery times than those of pure SnO_2 sensors. Therefore, F-doped SnO_2 sensor showed promising gas-sensing properties for ethanol gas.

This study found that F-SnO_2 sensor may be a remarkable gas sensor material for ethanol gas sensing.

7. Gas-sensing mechanism

Figures 11(a) and (b) demonstrate schematic band diagrams of Ag/SnO_2 in oxidized and reduced states, respectively. The ethanol gas-sensing mechanism of SnO_2 film can be explained as follows. The operation principle of SnO_2-based gas sensor lies in detecting the conductivity changes undergone by *n*-type material when surface-chemisorbed oxygen reacts with reducing gases, such as ethanol. In the simpler schematization of the detection mechanism, reasonably conductivity is low in clean air because the conduction electrons are bound to surface oxygen; whereas electrons are no longer bound to the surface states in presence of reducing gas, thereby, increasing conductivity. Therefore, the adsorption of gaseous species controls the surface and grain boundary resistance of the oxide. Considering gas adsorption is related to the surface of the material, polycrystalline and even nanocrystalline structures are preferred. First, oxygen is adsorbed onto the SnO_2 surface when the film is heated in air. The surface reactions at lower temperatures would proceed too slowly to be useful. The adsorption of oxygen forms ionic species, such as O_2^-, O_2^- and O^-, which have acquired electrons from the conduction band (E_c) and trapped the electrons on the surface as shown in figure 11(a) (Franke *et al* 2006). This occurrence creates band-bending and electron-depleted regions. Electron-depleted region is the so-called space-charge layer of which thickness is the length of the band-bending region. The reaction of these oxygen species with reducing gases or a competitive adsorption and replacement of the adsorbed oxygen by other molecules decreases and can reverse band-bending (figure 11(b)), resulting in increased conductivity. O^- is dominant at operating temperature range between 473 and 723 K (Yamazoe *et al* 1979), which is the working temperature for most metal oxide gas sensors. Thus, only O^- species will react with ethanol at temperatures where sensor studies have been carried out. The reaction kinematics is as follows:

$$O_2\ (\text{gas}) \Longleftrightarrow O_2\ (\text{adsorbed}),$$

$$O_2\ (\text{adsorbed}) + e^- \Longleftrightarrow O_2^-,$$

$$O_2^- + e^- \Longleftrightarrow 2O^-.$$

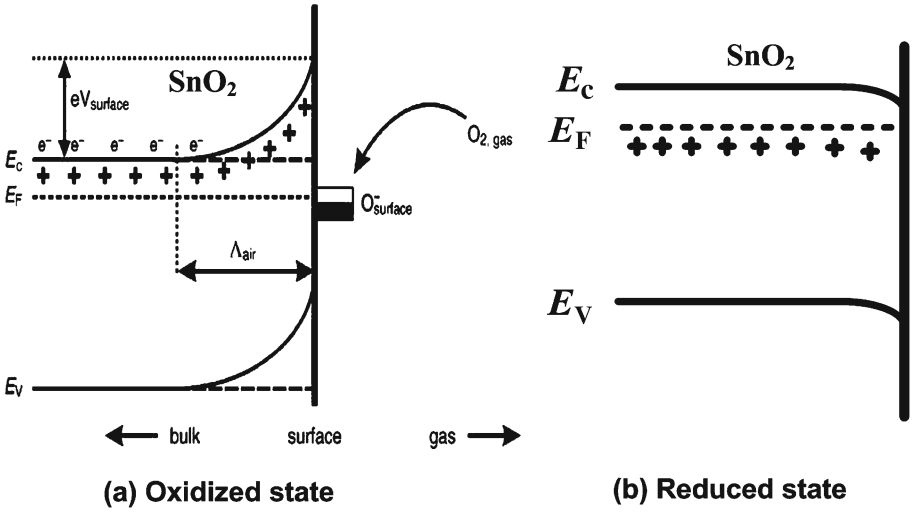

Figure 11. Schematic band diagrams of Ag/SnO_2 in (**a**) oxidized and (**b**) reduced states. Band bending after chemisorption of charged species (here ionosorption of oxygen). E_c, E_V and E_F denote energy of conduction band, valence band and Fermi level, respectively whereas Λ_{air} denotes thickness of space-charge layer and eV surface denotes potential barrier. Conducting electrons are represented by e^-; whereas + represents donor sites.

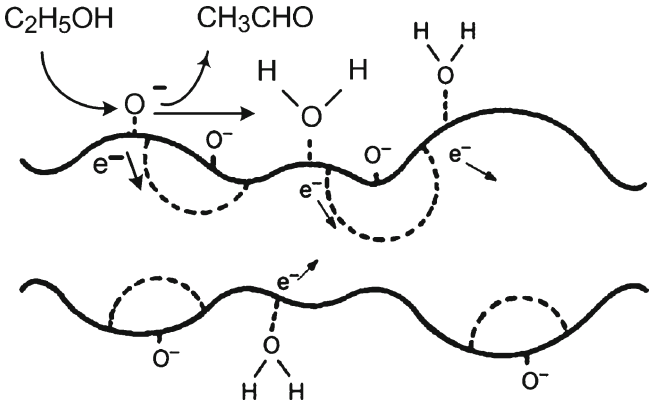

Figure 12. Schematic model of oxygen ionosorption on SnO_2 surface. Broadest conduction channel was observed at exposure to ethanol gas.

The reaction between ethanol and ionic oxygen species can take place in two different ways:

$$C_2H_5OH\,(\text{gas}) + O^- \Longleftrightarrow CH_3CHO\,(\text{g}) + H_2O\,(g/\text{ad}) + e^-,$$

$$C_2H_5OH\,(\text{gas}) \Longleftrightarrow H + C_2H_5O\,(\text{surface}),$$

$$C_2H_5O \Longleftrightarrow H + CH_3CHO,$$

$$CH_3CHO + O\,(\text{bulk}) \rightarrow CH_3COOH + O\,(\text{vacancies}).$$

The surface concentration of oxygen ions is decreased given its partial or complete oxidation (figure 12) when ethanol is introduced, releasing the trapped electrons to the bulk materials together with the decrease of the number of surface O^-. Subsequently, thickness of the space-charge layer decreases. Thus, Schottky barrier between two grains is lowered with reduced concentration of scattering centres, thereby increasing the electron mobility in the oxide. Hence, conducting electrons in sensing layers through different grains would be easy.

8. Conclusions

Ethanol and other reported hydrocarbon gas sensors are mainly based on SnO_2. SnO_2 films produced through a cost-effective sol–gel process with a high specific area coating is possible. Pure and nanocrystalline F-doped resistive gas sensors were fabricated with Ag contact. Surface morphology and crystalline property can be examined by SEM and XRD analyses. No correlation exists between sensitivity and film thickness considering the dominant role of the microstructure. The optical bandgap for pure SnO_2 film is 3·45 eV. Electrical investigations suggest that the resistivity of F-doped films decreases by more than 118 times in magnitude compared with pure SnO_2 films, which is of great significance for gas sensor fabrication and application. Thus F-doped SnO_2 sensors may present promising applications for the fabrication of gas sensors with low resistance and quick response (10 s) and recovery time (13 s), which would be much shorter than those of pure SnO_2 sensors.

Acknowledgements

The authors are thankful to the Department of Science and Technology (DST), New Delhi, for providing financial assistance to carry out this research work. The authors are also thankful to Mr A K Sharma, Satinder Singh, Sumit Thakur and Anubhav of CSIR–CSIO for their assistance in the sensor fabrication.

References

Acosta D R, Zirconi E P, Montoya E and Estrada W 1996 *Thin Solid Films* **288** 1
Aukkaravittayapun S, Wongtida N, Kasecwatin T, Charojrochkul S, Unnanon K and Chindaudom P 2006 *Thin Solid Films* **496** 117
Chang M S, Ryong K H, Graeme A, John D and Lee J-H 2008 *Sens. Actuators* **B131** 556
Chatterjee K, Chatterjee S, Banerjee A, Raut M, Pal N C, Sen A and Maiti H S 2003 *Mater. Chem. Phys.* **81** 33
Chaudhary V A, Mulla I S and Vijayamohanan K 1999 *Sens. Actuators* **B55** 154
Chen J, Wang K, Huang R, Saito T, Ikuhara Y H, Hirayama T and Zhou W 2010 *IEEE Trans. Nanotechnol.* **9** 634
Donato A, Della Corte F, Gioffrè M, Donato N, Bonavita A, Micali G and Neri G 2009 *Thin Solid Films* **517** 6184
Elangovan E and Ramamurthi K 2003 *J. Optoelectronics Adv. Mater.* **5** 45
Elangovan E, Singha M P, Dharmaprakash M S and Ramamurthi K 2004 *J. Optoelectronics Adv. Mater.* **6** 197
Epifani M, Díaz R, Arbiol J, Comini E, Sergent N, Pagnier T, Siciliano P, Faglia G and Morante J R 2006 *Adv. Funct. Mater.* **16** 1488
Esfandyarpour B, Mohajerzadeh S, Famini S, Khodadadi A and Asl Soleimani E 2004 *Sens. Actuators* **B100** 190
Eun H T and Ko Y S 2003 *J. Ind. Eng. Chem.* **9** 348
Franke M E, Koplin T J and Simon U 2006 *Small* **2** 36
Gordillo G, Moreno L C, de la Cruz W and Teheran P 1994 *Thin Solid Films* **252** 61
Gu Z, Liang P, Liu X, Zhang W and Le Y 2000 *J. Sol–Gel Sci. Technol.* **18** 159
Han C H, Han S D, Singh I and Toupance T 2005 *Sens. Actuators B* **109** 264
Han C H, Han S D and Khatkar S P 2006 *Sensors* **6** 492
Johnson V A and Horovitz K L 1947 *Phys. Rev.* **71** 374
Kamins T I 1971 *J. Appl. Phys.* **42** 4357
Korotcenkov G and Cho B K 2009 *Sens. Actuators B* **142** 321
Lampert C M 1982 *Ind. Eng. Chem. Prod. Res. Dev.* **21** 612
Leja E, Korecki J, Krop K and Toll K 1979 *Thin Solid Films* **59** 147
Li X-L, Lou T-J, Sun X-M and Li Y-D 2004 *Inorg. Chem.* **43** 5442
Mishra S, Ghanshyam C, Ram N, Singh S, Bajpai R P and Bedi R K 2002 *Bull. Mater. Sci.* **25** 231
Mohammed M T and Abdul Ghafor W A 1989 *Solid State Commun.* **72** 1043

Park S-S and Mackenzie J D 1996 *Thin Solid Films* **274** 154
Sakai G, Baik N S, Miura N and Yamazoe N 2001 *Sens. Actuators* **B77** 116
Seto J Y W 1975 *J. Appl. Phys.* **46** 5247
Shukla S, Agarwal R, Cho H J, Seal S, Ludwig L and Parish C J 2005a *J. Appl. Phys.* **97** 054307
Shukla S, Ludwig L, Parish C and Seal S 2005b *Sens. Actuators* **B104** 223
Steffes H, Imawan C, Solzbacher F and Obermeier E 2000 *Sens. Actuators* **B68** 249
Thangaraju B 2002 *Thin Solid Films* **402** 71
Varghese O K, Malhotra L K and Sharma G L 1999 *Sens. Actuators* **B55** 161
Vlachos D S, Skafidas P D and Avaritsiotis J N 1995 *Sens. Actuators* **B25** 491
Wada K and Egashira M 2000 *Sens. Actuators* **B62** 211
Xu C, Tamaki J, Miura N and Yamazoe N 1991 *Sens. Actuators* **B3** 147
Yamazoe N 1991 *Sens. Actuators* **B5** 7
Yamazoe N, Fuchigami J, Kishikawa M and Seiyama T 1979 *Surf. Sci.* **86** 335